



NRC Publications Archive Archives des publications du CNRC

Impact of Plasma-Sprayed Metal Particles on Hot and Cold Glass Surfaces

McDonald, A.; Lamontagne, M.; Moreau, C.; Chandra, S.

This publication could be one of several versions: author's original, accepted manuscript or the publisher's version. / La version de cette publication peut être l'une des suivantes : la version prépublication de l'auteur, la version acceptée du manuscrit ou la version de l'éditeur.

For the publisher's version, please access the DOI link below. / Pour consulter la version de l'éditeur, utilisez le lien DOI ci-dessous.

Publisher's version / Version de l'éditeur:

<https://doi.org/10.1016/j.tsf.2006.03.010>

Thin Solid Films, 514, 1-2, pp. 212-222, 2006-08-30

NRC Publications Record / Notice d'Archives des publications de CNRC:

<https://nrc-publications.canada.ca/eng/view/object/?id=b548a596-1dba-461a-8fe8-85372440e2e0>

<https://publications-cnrc.canada.ca/fra/voir/objet/?id=b548a596-1dba-461a-8fe8-85372440e2e0>

Access and use of this website and the material on it are subject to the Terms and Conditions set forth at

<https://nrc-publications.canada.ca/eng/copyright>

READ THESE TERMS AND CONDITIONS CAREFULLY BEFORE USING THIS WEBSITE.

L'accès à ce site Web et l'utilisation de son contenu sont assujettis aux conditions présentées dans le site

<https://publications-cnrc.canada.ca/fra/droits>

LISEZ CES CONDITIONS ATTENTIVEMENT AVANT D'UTILISER CE SITE WEB.

Questions? Contact the NRC Publications Archive team at

PublicationsArchive-ArchivesPublications@nrc-cnrc.gc.ca. If you wish to email the authors directly, please see the first page of the publication for their contact information.

Vous avez des questions? Nous pouvons vous aider. Pour communiquer directement avec un auteur, consultez la première page de la revue dans laquelle son article a été publié afin de trouver ses coordonnées. Si vous n'arrivez pas à les repérer, communiquez avec nous à PublicationsArchive-ArchivesPublications@nrc-cnrc.gc.ca.



National Research
Council Canada

Conseil national de
recherches Canada

Canada

Impact of plasma-sprayed metal particles on hot and cold glass surfaces

A. McDonald^{a,*}, M. Lamontagne^b, C. Moreau^b, S. Chandra^a

^a Center for Advanced Coatings Technology, Department of Mechanical and Industrial Engineering, University of Toronto, Toronto, Ontario, Canada M5S 1A4

^b National Research Council Canada, Industrial Materials Institute, Boucherville, Québec, Canada J4B 6Y4

Received 2 November 2005; received in revised form 18 January 2006; accepted 6 March 2006

Available online 17 April 2006

Abstract

Plasma-sprayed molten molybdenum and amorphous steel particles (38–55 μm diameter) were photographed during impact (velocity 120–200 m/s) and spreading on a smooth glass surface that was maintained at either room temperature or 400 °C. Droplets approaching the surface were identified by a photodetector and after a known delay, a 5-ns laser pulse was triggered to illuminate the spreading splat and photograph it with a charge-coupled device (CCD) camera. A rapid two-color pyrometer was used to collect thermal radiation from particles during flight and impact to follow the evolution of their temperature and size. Particles that impacted the surface at room temperature ruptured and splashed, leaving a small central solidified core on the substrate. On a surface held at 400 °C, there was no splashing and a circular, disk-like splat remained on the surface. Splats on a glass surface held at room temperature had a maximum spread diameter almost three times that on a hot surface. A simple analysis was done to estimate the area of the splat in contact with the non-heated glass surface during spreading. The analysis supports the hypothesis that only a portion of the splat is in good contact with the surface at room temperature, while the rest of the fluid is separated from the substrate by a gas barrier.

© 2006 Elsevier B.V. All rights reserved.

Keywords: Contact area; Gas barrier; Splashing; Two-color pyrometry

1. Introduction

Fundamental studies of plasma-spray coating processes have found that the temperature of the substrate on which molten droplets impact influences their morphology, size, and extent of splashing [1–6]. Splat morphology affects coating properties such as porosity, adhesion strength, and microstructure [2,7]. Aziz and Chandra [8] showed that, for low velocity impacts of tin (1–4 m/s) on mirror-polished stainless steel held at room temperature, as the droplet impact velocity increased, the maximum diameter of the splat increased, and was accompanied by significant splashing. Several investigators [2,6] have found that, for plasma-sprayed particles, increasing substrate temperature reduced the occurrence of splashing and produced disk-like splats. Jiang, et al. [9] have shown also that removal of condensates and/or adsorbates from a cold stainless steel substrate will eliminate splashing and splat fragmentation

of impacting molten zirconia and produce contiguous, disk-like splats.

Many images of the impact and spreading of droplets on flat surfaces have been captured for low velocity impacts [8]. However, it is difficult to capture clear images of the spreading particles in the actual plasma-spray process. Mehdizadeh et al. [5] have photographed plasma-sprayed molybdenum droplets impacting cold glass by using a charge-coupled device (CCD) camera and long-range microscope. A high-speed two-color pyrometer was also used to obtain the temperature evolution during spreading. The two-color pyrometric method, as described by Fantassi et al. [10] and Gougeon et al. [11], calculates the splat temperature from the ratio of the intensities of radiation collected at two different wavelengths. A similar method was employed by Cedelle et al. [12] to photograph the different splashing phenomena of millimeter-sized, plasma sprayed yttria-stabilized zirconia on stainless steel substrates. A CCD camera was oriented either parallel to the cold substrate to photograph the impact splashing or orthogonal, to photograph the splashing during flattening. Tiny droplets were ejected immediately after particle impact during impact splashing,

* Corresponding author.

E-mail address: mcdonald@mie.utoronto.ca (A. McDonald).

while during flattening splashing, the splat disintegrated during spreading on the substrate. It was found that splashing seemed to occur immediately after impact and continued during flattening.

Fukumoto et al. [2] found that the microstructure of nickel and copper splats on heated AISI 304 steel substrates was fine, columnar, flat, and non-porous, while on the cold steel, it was composed of isotropic coarse grains, indicating that the cooling rate of the splats on the hot substrate was larger than that on the cold substrate. However, actual temperatures during the cooling of the splat were not measured. Moreau et al. [4] measured the temperature evolution of molybdenum droplets that impacted and spread on cold and hot glass. It was found that the cooling rate of the splats on hot glass was on the order of 10^8 K/s, an order of magnitude larger than the splats on cold glass (10^7 K/s). Bianchi et al. [13] used a 1-D splat cooling model to show that the thermal contact resistance at the interface of yttria-stabilized zirconia splats and polished stainless steel substrates affects the splat cooling rate significantly. It was found that as the thermal contact resistance increased, the cooling rate decreased.

Photographing droplets in a plasma spray at different stages during impact gives insight into the dynamics of splat formation on both hot and cold substrates. Fukumoto et al. [2,3] have speculated that during impact on a non-heated surface, only the central portion of the splat is in good contact with the surface, while the rest of the fluid jets out over a gas layer and splashes. However, no direct experimental evidence is available to test this hypothesis.

The objectives of this study were to: (1) use a rapid CCD camera to photograph molybdenum and amorphous steel particles that impacted glass held at room temperature and at 400°C ; (2) use high speed two-color pyrometry to measure the temperature and size evolutions of molybdenum and amorphous steel particles after collision and during spreading; and (3) estimate the area of the splat in contact with the non-heated glass surface during spreading.

2. Experimental details

A schematic diagram of the experimental setup is shown in Fig. 1. A SG100 torch (Praxair Surface Technologies, Indianapolis, IN) was used to melt and accelerate dense, spherical molybdenum (SD152, Osram Sylvania Chemical and Metallurgical Products, Towanda, PA) and amorphous steel (44% Cr, 48% Fe, 6% B, 2% Si, traces of C and S) (LMC-M, Liquidmetal Technologies, USA) powder particles, sieved to $-60+38\mu\text{m}$, with an average diameter of $40\mu\text{m}$. The powder feed rate was less than 1 g/min. It has been shown that the steel powder particles are composed of an amorphous phase and, after plasma-spraying and solidification, the splats exhibit a high amorphous content [14]. The plasma torch was operated with a voltage of 35 V and a current of 700 A. The plasma gas mixture was argon at a flow rate of 50 liters per minute (LPM) and helium at 24.5 LPM. The substrate was a glass microscope slide (Fisher Scientific, Pittsburgh, PA) that was washed with water and ethanol and dried in an oven at 140°C for 1800 s. In

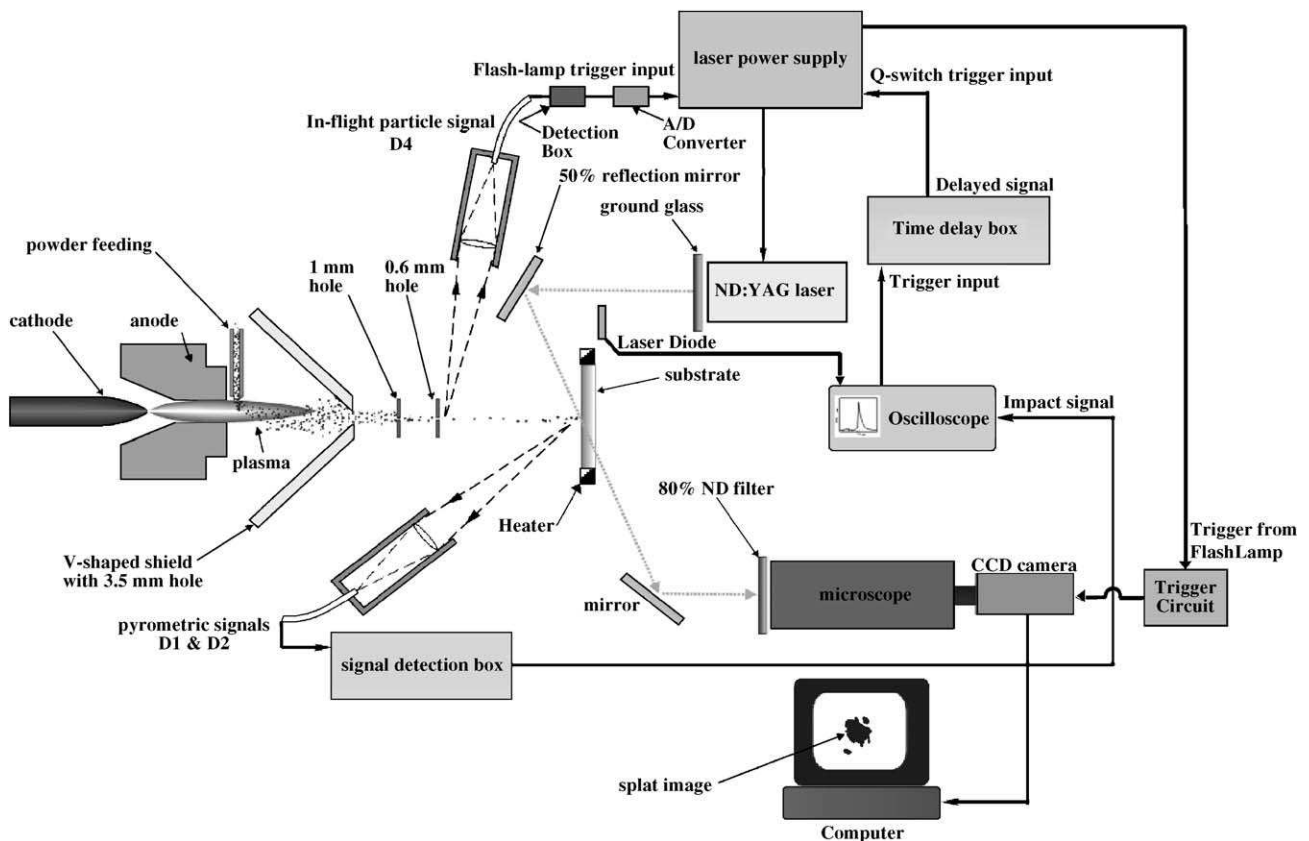


Fig. 1. Schematic of the experimental assembly.

order to heat the substrate, the glass was placed in a copper substrate holder that included resistance heater wires.

The plasma torch was passed rapidly across the glass substrate. In order to protect the substrate from an excess of particles and heat, a V-shaped barrier was placed in front of the torch. This V-shaped shield had a 3.5-mm hole in it through which particles could pass. To reduce the number of particles landing on the substrate, two additional barriers were placed in front of the substrate, the first of which had a 1-mm hole and the second, a 0.6-mm hole. All the holes were aligned to permit passage of the particles with a horizontal trajectory.

After exiting the third barrier and just before impacting the substrate, the thermal radiation of the particle was measured with a rapid two-color pyrometric system. This system included

an optical sensor head that consisted of a custom-made lens, which focused the collected radiation, with 0.21 magnification, on an optical fiber with an 800- μm core [11]. This optical fiber was covered with an optical mask that was opaque to near infrared radiation, except for three slits (see Fig. 2A). The two smaller slits (slits b and c in Fig. 2A), with dimensions of 30 μm by 150 μm and 30 μm by 300 μm , were used to detect the thermal radiation of the in-flight particles. The radiation was used to calculate the temperature and velocity of the in-flight particle [11,15]. The largest slit (slit e in Fig. 2A), measuring 150 μm by 300 μm , was used to collect thermal radiation of the particle as it impacted and spread on the substrate. With the thermal radiation from this slit, the splat temperature, diameter, and cooling rate were calculated at 100-ns intervals after impact.

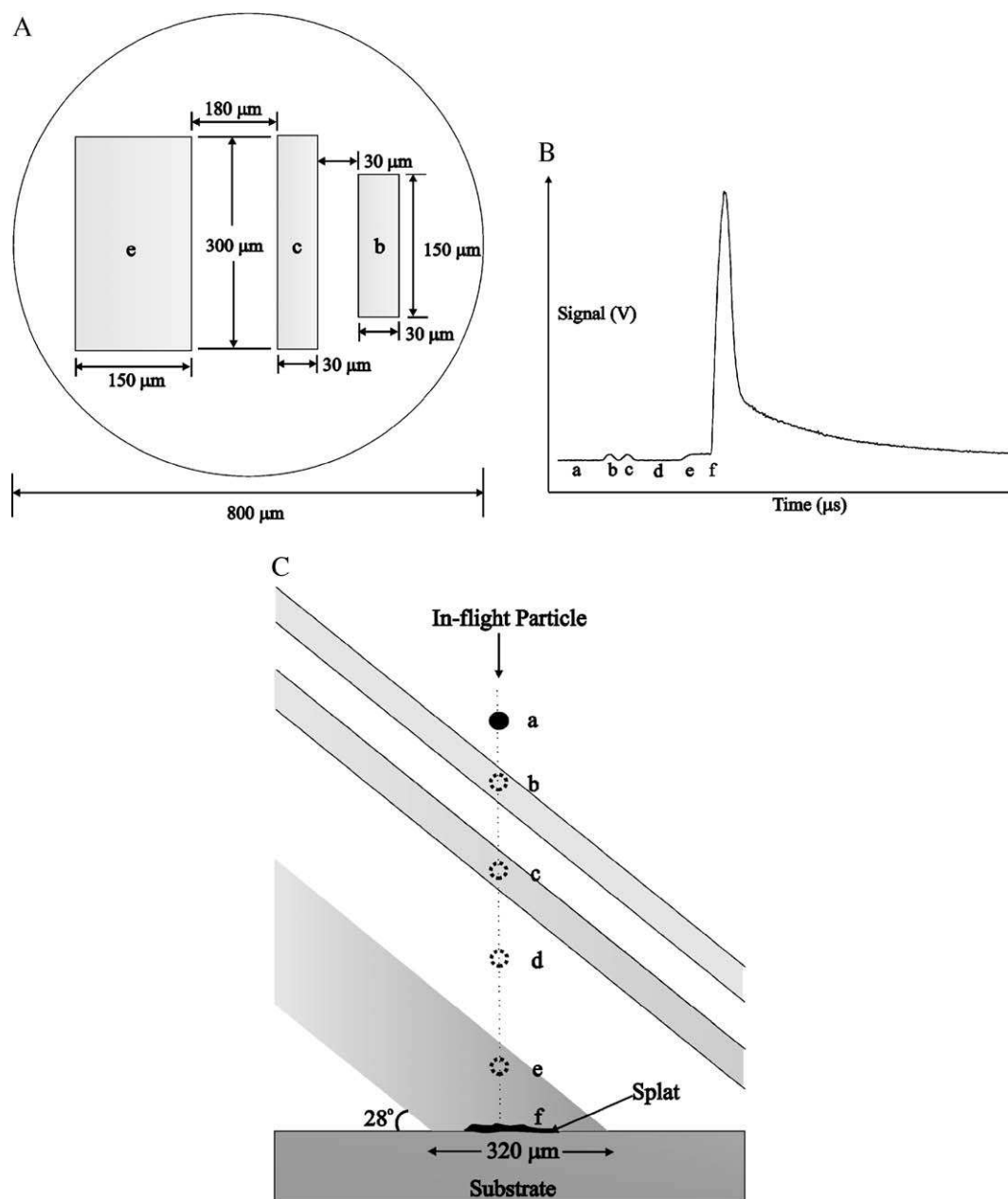


Fig. 2. (A) Details of the three-slit mask. (B) A typical signal collected by the three-slit mask. (C) Schematic of the optical detector fields of view.

The collected thermal radiation was transmitted through the optical fiber to a detection unit that contained optical filters and two photodetectors. The radiation beam was divided into two equal parts by a beam splitter. Each signal was transmitted through a bandpass filter with wavelength of either 785 nm or 995 nm and then detected using an avalanche silicon photodetector. The ratio of the radiation intensity at these wavelengths (referred to as D_1 and D_2 , respectively) was used to calculate the particle temperatures with an accuracy of $\pm 100^\circ\text{C}$ [15]. The signals were recorded and stored by the digital oscilloscope. A signal from the laser diode in Fig. 1 was also stored by the oscilloscope. This indicated the time in which the splat image was captured, relative to the pyrometric signals.

Fig. 2B shows a typical signal captured by a photodetector. The labels, a–f, correspond to the position of a particle (shown in Fig. 2C) as it passes through the fields of view of each of the

optical slits. At points a and d, the particle was not in the optical field of view of any of the slits, so the signal voltage was zero. The two peaks at points b and c were produced by thermal emissions from the particle as it passed through the first two small slits. The droplet average in-flight velocity was calculated by dividing the known distance between the centers of the two slits by the measured time of flight. At point e the droplet entered the field of view of the third and largest optical slit. This is shown on the thermal signal by a plateau in the profile. Upon impact at f, the signal increased as the particle spread and eventually decreased as the particle cooled down and/or splashed out of the field of view.

To illuminate an impacting particle, a 5 ± 2 ns duration pulse of light from a Nd:YAG laser (Continuum Minilite, Santa Clara, CA) was used. Since the flashlamp of the laser had to be triggered at least $150\mu\text{s}$ before it was pulsed, an optical sensor

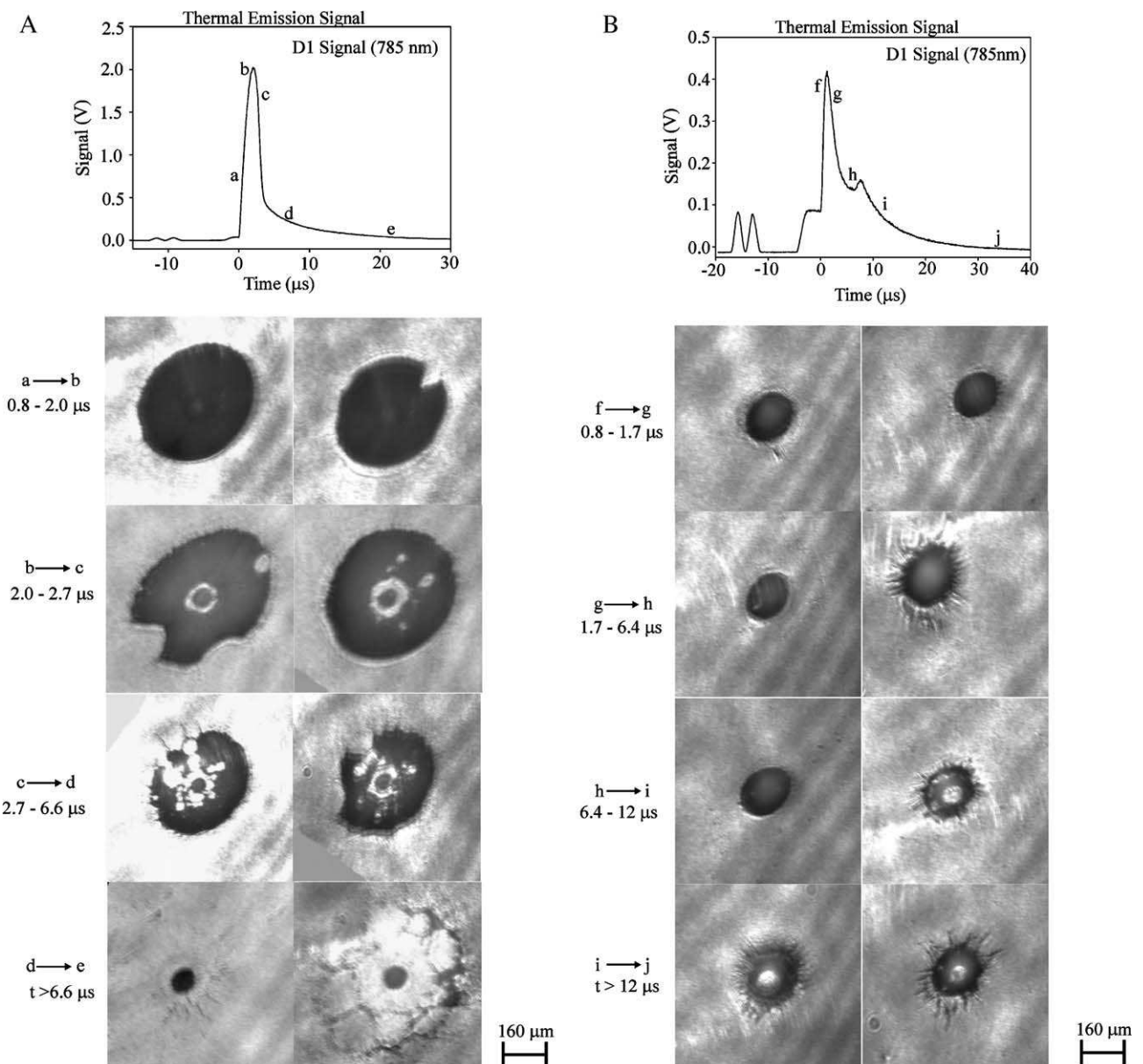


Fig. 3. Typical thermal emission signals and images of molybdenum splats at different times after impact on glass held at (A) room temperature and (B) 400°C .

(labelled D_4 in Fig. 1) was positioned to detect thermal radiation from a particle immediately after it exited the 0.6-mm hole in the third shielding plate. The signal was used to trigger the flashlamp on the laser power supply/control box. When the particle entered the large slit field of view (labeled e in Fig. 2A) of the optical fiber, a signal was sent to trigger the laser after a controlled time delay. This permitted illumination of the substrate at different time intervals after impact and during spreading of the droplet. Since the pulse was about three orders of magnitude smaller than the spreading time of the droplet ($\sim 1\text{--}2\mu\text{s}$), blurs in the images of these high speed particles were eliminated.

A 12-bit CCD camera (QImaging, Burnaby, BC) was used to capture images of the spreading particles from the back of the glass substrate. The electronic shutter of the camera was triggered to open by a signal from the flashlamp of the laser. The camera was connected to a long-range microscope (Astro-optics Division, Montpelier, MD) that had an 80% neutral density (ND) filter to attenuate the intensity of the laser beam. The images captured by the camera were digitized by a frame grabber and recorded on a personal computer. Since the images were not photographed directly, but rather, their reflection in a mirror that was at an angle relative to the substrate, the digitized images were rotated and shortened on both dimensions. The degree of foreshortening was determined by photographing a circular aperture of known diameter placed on the glass. The images were rotated 60° counter-clockwise (CCW), the widths were shortened by 75%, and the heights were shortened by 68%. The captured images corresponded to individual splats at specific times after impact and during spreading. The images were arranged in sequence, based on the time after impact, to show the general morphology of the splats during spreading.

3. Results and discussion

3.1. Thermal emission signals and images of spreading splats

Fig. 3 shows images of molybdenum splats at different times after impact on glass held at room temperature or at 400°C . The figure also shows typical D_1 thermal emission signals. D_2 thermal emission signals have the same shape and are not shown. For molybdenum, the average droplet impact velocity was $135\pm 2\text{ m/s}$ and the average temperature of the in-flight particles were $2975\pm 10^\circ\text{C}$, well above the melting point (2617°C). 37 samples were available for analysis. The statistical errors, calculated by dividing the standard deviation by the square-root of the number of samples, are shown with the averages. The statistical errors will be reported with the averages of all other parameters mentioned in this study.

The photodetector signal of impact and spread on the glass held at room temperature was subdivided into four intervals (indicated by labels a–e in Fig. 3A) and photographs taken in each of these time periods are grouped together in Fig. 3A. The approximate time after impact that corresponds to each interval is shown in the figure. To demonstrate the repeatability of the process, two splat images are shown during each time interval.

The a to b range represents splats immediately before or upon achieving the average maximum spread diameter of $370\pm 20\mu\text{m}$ (for 17 samples). The maximum spread diameter was obtained by using the ImageJ imaging software (National Institutes of Health, Washington, DC). The area and perimeter of the splat at the maximum extent, before break-up, were determined by the software and the diameter was calculated from the hydraulic diameter formula, $D = \frac{4A_c}{P}$. Beyond point b, the liquid portion of the splats begins to disintegrate, initially from the solidified central core and later, from sites within the liquid film. After point d, the splat is almost totally disintegrated and only a central solidified core remains on the glass.

Fig. 3B shows the results after impact on a glass substrate at 400°C . There was almost no splat break-up or splashing, unlike that seen in Fig. 3A. Also, the average diameter of the splat increased to a maximum of $130\pm 8\mu\text{m}$ after impact (for 20 samples), much less than that on a cold surface ($370\mu\text{m}$). At point h on the pyrometric signal, there is a voltage decrease, followed by an increase that begins about $4\mu\text{s}$ after impact. This is typical of the spreading splats on the hot glass and represents the onset of liquid solidification. Pyrometric measurements of the splat temperature during spreading on the heated glass (Fig. 4) showed that the time period around point h corresponded to a period of almost constant splat temperature, indicating recalescence and solidification, which began about $4\mu\text{s}$ after impact. In this case, during recalescence, the splat temperature fell below the melting point and was raised, as the latent heat of fusion is released, until solidification was complete, instead of until reaching the

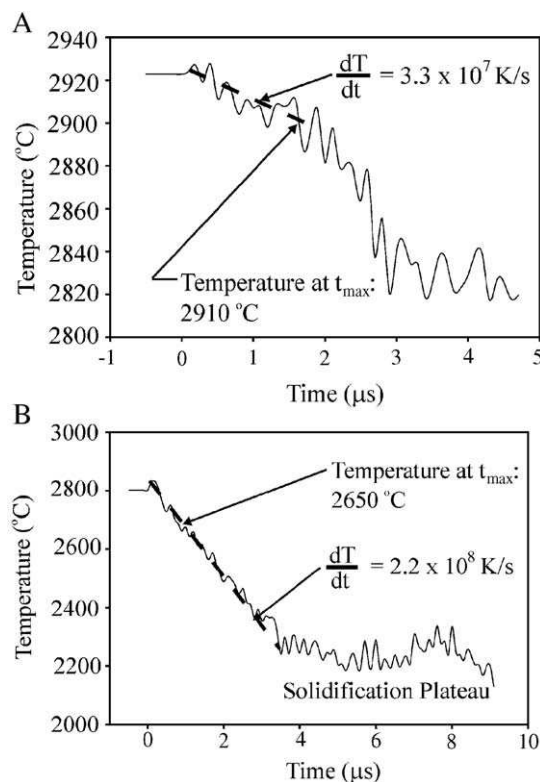


Fig. 4. Typical cooling curves of molybdenum splats on glass held at (A) room temperature and (B) 400°C .

fusion point [16]. After complete solidification, the temperature began to decrease again as the splat cooled further. This phenomenon is not observed on the pyrometric signal of the splats on non-heated glass (Fig. 3A). Moreau et al. [17] have shown that, for molybdenum, splat material loss begins approximately $3\mu\text{s}$ after impact, when the molten material exits the pyrometric field of view. Pyrometric measurements of the temperature (Fig. 4A) show that the splat temperature at this time is approximately 2800°C , well above the molybdenum melting point (2617°C). On the pyrometric signals, recalcence is not observed because a large portion of the splat has exited the field of view before solidifying.

The time required for the splat to spread to its maximum diameter after impact was measured starting at the instant the pyrometric thermal emission signals began to increase after the plateau (point f of Fig. 2B) to the maximum voltage on the thermal emission signal profile. For molybdenum on glass

held at room temperature, the average maximum spread time was $2\pm 0.07\mu\text{s}$ and on glass held at 400°C , it was $1\pm 0.05\mu\text{s}$.

Fig. 5 shows similar results for steel droplets at different time periods after impact on glass held at room temperature and at 400°C . The average impact velocity was $175\pm 3\text{ m/s}$ and the average temperature of the in-flight particles was $3060\pm 220^\circ\text{C}$, well above the temperature at which steel completely melts (1550°C). 17 samples were available for analysis. The splat morphologies and spread dynamics of amorphous steel closely resemble those of molybdenum.

For amorphous steel, the average maximum spread diameter of the splats on cold glass was $375\pm 10\mu\text{m}$ (for 11 samples); while on hot glass it was $125\pm 1\mu\text{m}$ (6 samples). Instead of splashing, splats on the hot surface appear to recoil after achieving the maximum spread diameter and become smaller as observed in sequence h to i of Fig. 5B. This was possibly due to surface tension forces that pull back on the liquid. The average

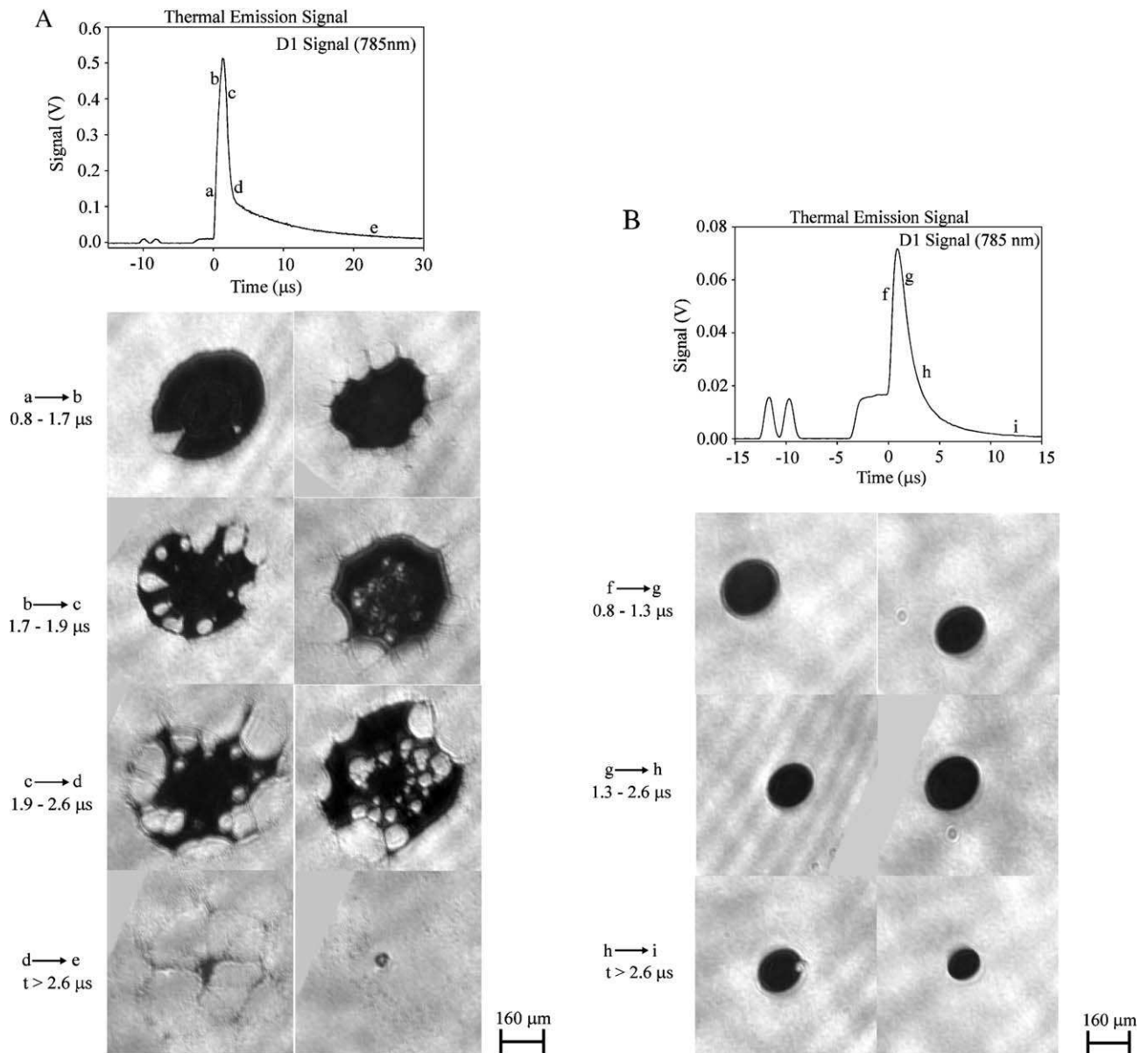


Fig. 5. Typical thermal emission signals and images of amorphous steel splats at different times after impact on glass held at (A) room temperature and (B) 400°C .

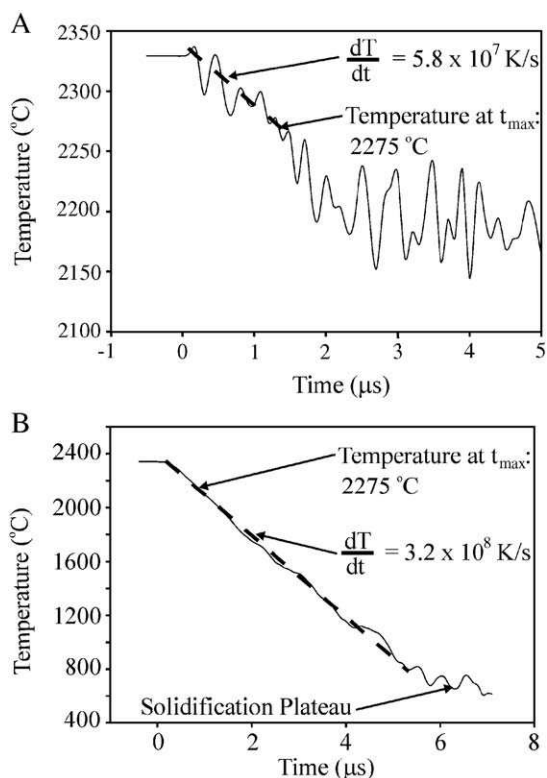


Fig. 6. Typical cooling curves of amorphous steel splats on glass held at (A) room temperature and (B) 400 °C.

maximum spread times of this material on cold glass was $1.5 \pm 0.07 \mu\text{s}$ and on hot glass, it was $0.8 \pm 0.03 \mu\text{s}$.

Unlike molybdenum, the thermal emission signals of amorphous steel splats on hot glass did not show a period of recalescence (Fig. 3B). For single component, pure substances such as molybdenum, recalescence will be observed as the material solidifies and crystallizes. An amorphous alloy will not show a period of recalescence because this material does not crystallize during solidification.

Analysis of the images indicates that the maximum spread diameter of the splats on the cold glass are approximately three times that on the hot glass for both the pure metal and the alloy. An image that shows a splat at the maximum spread extent is one that was taken at the time when the thermal emission signal was a maximum. That may be observed in sequences b to c and f to g of Figs. 3 and 5.

3.2. Cooling curves of molybdenum and amorphous steel

The evolution of the liquid temperature during the spreading of molybdenum and amorphous steel splats on cold and hot glass are illustrated in Figs. 4 and 6, respectively. The temperatures were calculated from the ratio of signals from the photodetectors, D_1 and D_2 , and an experimentally determined calibration equation. Shinoda et al. [18,19] also used a two-color pyrometric method to prepare graphs of the temperature evolution of plasma-sprayed yttria-stabilized zirconia on heated quartz glass. In the figures (Figs. 4 and 6), the slope of the curves, $\frac{dT}{dt}$, represents the average splat cooling

rate calculated from all available splats. Table 1 shows the average cooling rates of the splats and the statistical errors. For molybdenum splats on non-heated glass, the splat cooling rate ranged from $1.5 \times 10^7 \text{ K/s}$ to $4.5 \times 10^7 \text{ K/s}$, while on heated glass, it ranged from $14 \times 10^7 \text{ K/s}$ to $35 \times 10^7 \text{ K/s}$. For amorphous steel splats on non-heated glass, the cooling rate varied from $2 \times 10^7 \text{ K/s}$ to $9.5 \times 10^7 \text{ K/s}$, while on heated glass, it ranged from $30 \times 10^7 \text{ K/s}$ to $40 \times 10^7 \text{ K/s}$. Since, on glass held at room temperature, fragmentation and splashing were observed after achieving the maximum spread diameter (Figs. 3 and 5), the cooling rate of the liquid splat was calculated from the time of impact to the point of initial disintegration of the splat ($\sim 2\text{--}3 \mu\text{s}$ after impact). On glass held at 400 °C, the degree of splashing was small, so the cooling rate of the liquid splat was calculated from the time of impact to the solidification plateau.

For both materials, the liquid cooling rates on glass held at 400 °C is approximately an order of magnitude larger (order of 10^8 K/s) than on the glass held at room temperature (order of 10^7 K/s). This suggests that thermal contact resistance between the cold glass and the splat is greater than that between the hot glass and splat. The cause of the increased thermal contact resistance on the cold surface is probably a gas barrier [20,21], formed after evaporation of adsorbed substances on the substrate beneath the splat. It is possible that heating the surface removes the adsorbed substances and gas barrier, producing better contact [2,9,22,23].

The cooling curves of the splats on glass held at 400 °C show the solidification plateau at temperatures lower than the melting point of the materials. For molybdenum, with melting point at 2617 °C, the solidification plateau occurs at approximately 2200 °C. For amorphous steel, complete solidification occurs at approximately 700 °C, but the melting point is approximately 1550 °C. The occurrence of solidification at temperatures lower than the melting point, coupled with large cooling rates on the order of 10^8 K/s , is evidence that undercooling of the splats occurred. It has been found that undercooling occurred when molybdenum particles impacted previously deposited hot splats [24]. The columnar microstructure of the splats in contact with previously deposited splats or a heated substrate indicated that the cooling rate was larger than that of the splats on the bare, cold substrate [2,24].

3.3. Maximum spread factor from thermal emission signals

The maximum spread factor is the maximum splat diameter normalized by the initial droplet diameter, $\xi_{\text{max}} = \frac{D_{\text{max}}}{D_0}$. The maximum spread factor can be determined by measuring directly the maximum splat diameters from the images and comparing those measurements to the in-flight droplet diameter.

Table 1
Average cooling rates of molybdenum and amorphous steel splats

Material	Glass temperature (°C)	No. of samples	$dT/dt \times 10^7 \text{ (K/s)}$
Molybdenum	27	17	3.3 ± 0.2
	400	20	22 ± 1.2
Amorphous steel	27	11	5.8 ± 0.8
	400	6	32 ± 1.7

However, only about 10% of the splat images were captured at the time when the thermal emission signal was at a maximum. Gougeon and Moreau [11] described a method of estimating the maximum spread factor directly from the thermal emission signal profiles. The maximum spread factor is calculated by comparing the maximum thermal emission signal of the splat obtained from the large, third-slit field of view (labelled e in Fig. 2A) to that obtained from any one of the smaller fields of view for the in-flight droplet (labelled b and c in Fig. 2A). Fig. 2C shows that the angle of detection is 28° . When the particle is in-flight, it is a sphere, so the particle area calculated from the thermal emission signal is independent of the angle of the detector and fields of view. When the particle impacts the substrate and forms a flat disk-shaped splat (at point f in Fig. 2C), the measured thermal emission signal will correspond to a projected area and will be dependent on the detector angle. To determine the true splat surface area to calculate the maximum spread factor, the observed maximum thermal emission signal will be corrected by taking into account the orientation of the detector. Since ξ_{\max} is a ratio of diameters and the thermal emission signal corresponds to surface area, the experimental maximum spread factor is obtained from the thermal emission signals as

$$\xi_{\max} = \sqrt{\frac{S_{\max, \text{measured}} * \frac{1}{\sin 28^\circ}}{S_{\text{IF}}}} \quad (1)$$

where S_{IF} is the thermal emission signal of the in-flight particle and $S_{\max, \text{measured}}$ is the observed thermal emission signal of the splat at the maximum extent.

Table 2 shows the average maximum spread factors ($\bar{\xi}_{\max}$) of molybdenum and amorphous steel that impacted glass at room temperature and at 400°C . The maximum spread factors were obtained from the splat thermal emission signals and from direct measurement of the maximum splat diameter from the images (Figs. 3 and 5). All available samples were considered to calculate mean spread factors from the thermal emission signals. At least two images of the splat at the maximum extent were available to measure the maximum spread diameter for each material, except for amorphous steel on glass at room temperature, where only one sample was available.

The maximum spread factors obtained from the thermal emission signals are in good agreement with those obtained from direct measurements of the images. The results show that the maximum spread diameter of the splats on cold glass is approximately three times that on glass at 400°C . Previous studies of molybdenum impact by Moreau et al. [4] have produced similar results.

Table 2
Average maximum spread factors of molybdenum and amorphous steel splats

Material	Glass temperature ($^\circ\text{C}$)	No. of samples	$\bar{\xi}_{\max}$ (from signals)	$\bar{\xi}_{\max}$ (from images)
Molybdenum	27	17	9.8 ± 0.2	9.4 ± 0.5
	400	20	3.4 ± 0.2	3.4 ± 0.2
Amorphous Steel	27	11	9.6 ± 0.3	8.9
	400	6	3.0 ± 0.2	3.2 ± 0.01

Table 3

Average maximum spread times of molybdenum and amorphous steel splats

Material	Glass temperature ($^\circ\text{C}$)	No. of samples	t_{\max} (μs)
Molybdenum	27	17	2.0 ± 0.07
	400	20	1.0 ± 0.05
Amorphous steel	27	11	1.5 ± 0.07
	400	6	0.8 ± 0.03

3.4. Analysis of droplet spread

Experiments have shown that heating the substrate has two clearly visible effects on splat impact: (a) splat cooling rates are much higher (see Table 1); and (b) the extent of splat spreading is much less (see Table 2). As a consequence of larger spread diameters, the time (t_{\max}) taken for droplets to spread to their maximum extent is also greater on a cold surface. Table 3 shows the average maximum spread times of molybdenum and amorphous steel on surfaces at both 27°C and 400°C .

Fukumoto et al. [3] and Jiang et al. [9] have previously proposed a mechanism that explains the differences between impact on hot and cold surfaces: a gas barrier, created by volatile substances evaporating from the cold surface during particle impact, prevents the splat from wetting the substrate. Only the centre of the splat, where the impact pressure is highest and the liquid is compressed [25], makes good contact with the cold substrate and leaves a solidified core adhering to the glass (Figs. 3 and 5), while the remainder breaks up and flies off the surface. Fig. 7 shows a schematic diagram of this proposed impact scenario. Fig. 8 shows photographs of the central cores that remain on the non-heated glass after particle spreading and solidification. The extent of splat spreading can be seen in Fig. 8A from the streaks surrounding the central core. Table 4 shows the average core diameters and the corresponding statistical errors of molybdenum and amorphous steel on non-heated glass.

On heated glass, it is speculated that surface contaminants evaporate prior to impact and there is good contact between the molten metal and glass over the entire surface of the splat. Cooling rates are therefore much greater, and the entire splat adheres to the substrate.

A simple energy conservation model, to predict the extent of droplet spreading during impact [8,26], offers support for this hypothesis, by giving an estimate of the splat area in contact

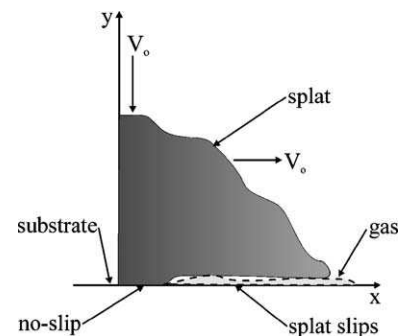


Fig. 7. Schematic of a typical splat spreading on glass held at room temperature.

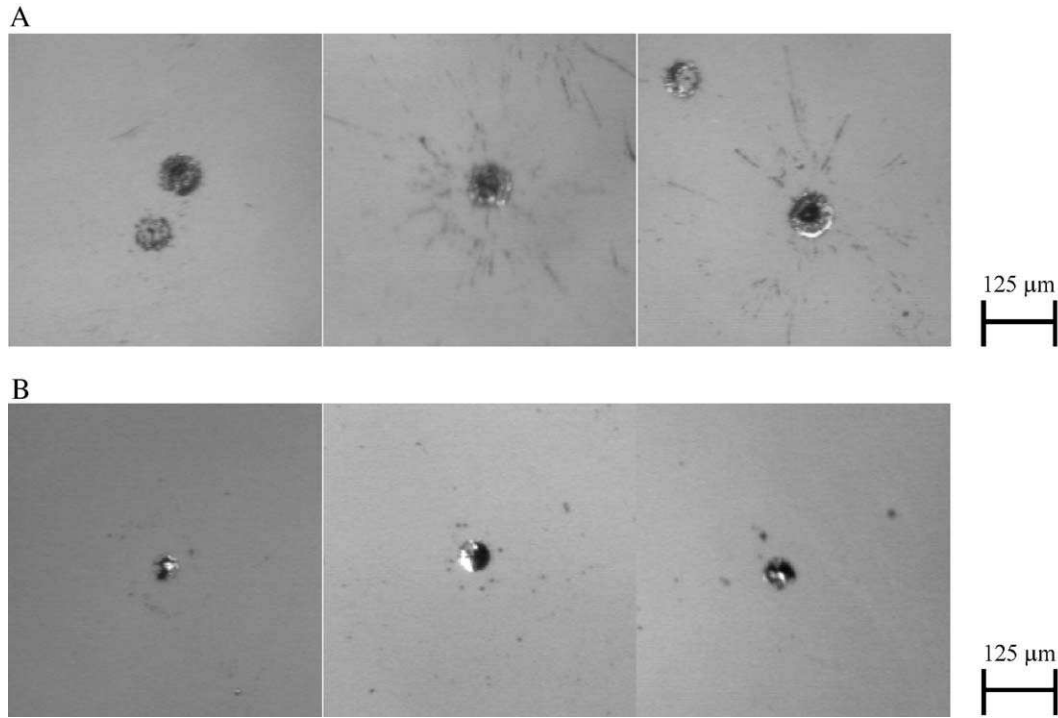


Fig. 8. Images of the solidified central cores of (A) molybdenum and (B) amorphous steel remaining on the substrate after impact.

with the substrate. The kinetic energy (KE_o) and surface energy (SE_o) of a droplet are

$$KE_o = \frac{1}{12} \pi \rho D_o^3 V_o^2, \quad (2)$$

$$SE_o = \pi D_o^2 \sigma. \quad (3)$$

Comparison of kinetic and surface energies of typical plasma-sprayed particles shows that $KE_o \gg SE_o$, so the initial surface energy will be neglected in this analysis. After impact, and when the splat is at its maximum diameter, D_{max} , the kinetic energy is zero and the surface energy (SE_1) is:

$$SE_1 = \frac{\pi}{4} D_{max}^2 \sigma (1 - \cos \theta) \approx \frac{\pi}{2} D_{max}^2 \sigma. \quad (4)$$

In Eq. (4) the advancing contact angle, θ , was assumed to be 180° .

According to Chandra and Avedisian [26], the approximate work done by the splat to overcome viscosity is

$$W \approx \phi \Omega t_{max}, \quad (5)$$

where t_{max} is the time required for the splat to spread to the maximum extent, Ω is the volume of the viscous fluid, and ϕ is

the viscous dissipation function. The order of magnitude of ϕ may be estimated by [26]

$$\phi \sim \mu \left(\frac{V_o}{L_c} \right)^2, \quad (6)$$

where μ is the dynamic viscosity of the liquid splat and L_c is the characteristic length, in the y -direction, over which viscous dissipation occurs. If the splat at its maximum extent is assumed to be a disk, then $\Omega = A_{vd} L_c$, where A_{vd} is the area of the splat in contact with the surface that loses energy by viscous dissipation. Substituting Eq. (6) and the volume expression into Eq. (5) gives the viscous dissipation energy,

$$W \sim \mu \frac{V_o^2}{L_c} A_{vd} t_{max}. \quad (7)$$

The conservation of energy condition between the droplet and the splat at the maximum extent, $KE_o = SE_1 + W$, and Eqs. (2), (4) and (7) gives a simple analytical expression for the area of the splat that is in contact with the substrate and loses energy by viscous dissipation as:

$$A_{vd} = \frac{\pi L_c (\rho D_o^3 V_o^2 - 6 D_{max}^2 \sigma)}{12 \mu V_o^2 t_{max}}. \quad (8)$$

Assuming that the impact parameters (D_o , L_c , V_o) and physical properties (μ , σ) of the particles are approximately the same for impact on both hot and cold surfaces, the ratio of the splat contact areas on the hot and cold surfaces is,

$$\frac{A_{vd,cold}}{A_{vd,hot}} = \frac{(\rho D_o V_o^2 - 6 \zeta_{max,cold}^2 \sigma) t_{max,hot}}{(\rho D_o V_o^2 - 6 \zeta_{max,hot}^2 \sigma) t_{max,cold}}. \quad (9)$$

Table 4
Average core diameters of molybdenum and amorphous steel splats

Material	No. of samples	D_c (μm)
Molybdenum	25	80 ± 4
Amorphous steel	31	70 ± 2

Table 5
Contact area ratio of molybdenum and amorphous steel splats

Material	From experiments (Eq. (10))	From analysis (Eq. (9))
Molybdenum	0.37	0.42
Amorphous steel	0.34	0.47

If we assume that only the core area is in contact with the substrate during impact and spreading on an unheated surface, the area ratio is:

$$\frac{A_{\text{vd,cold}}}{A_{\text{vd,hot}}} = \left(\frac{D_{\text{c,cold}}}{D_{\text{max,hot}}} \right)_{\text{exp}}^2 \quad (10)$$

Experimentally measured values of $D_{\text{c,cold}}$ and $D_{\text{max,hot}}$ were substituted in Eq. (10). Property values of molybdenum and amorphous steel were found elsewhere [27,28]. The properties of amorphous steel (44% Cr, 47.9% Fe, 5.9% B, 2% Si, 0.17% C and 0.03% S) are weighted averages of the properties of chromium and iron only. Table 5 shows a comparison between the predicted contact area ratio obtained from Eq. (9) and the experimental contact area ratio estimated from Eq. (10). Calculation of the circular diameter from the ratio obtained from the analysis and Eq. (9) (Table 5) shows that the diameter of the contact area of molybdenum is 90 μm and for amorphous steel, it is 80 μm . Table 4 shows that the measured core diameters were 80 μm and 70 μm for molybdenum and amorphous steel, respectively. Pasandideh-Fard et al. [29] used a similar conservation of energy method and similar simplifying assumptions to estimate the maximum spread factors of various droplets, with impact velocities between 1 and 4 m/s, to within 20% of experimental data. This, coupled with the agreement between the measured and predicted core diameters, confirms the accuracy of this method. The agreement between the predicted and measured values (see Tables 4 and 5) also suggest that for impact on a cold surface, the area in contact with the substrate is only slightly greater than that of the central core: the peripheral fluid is separated from the substrate by a possible gas barrier and does not lose much energy due to viscous dissipation. The splat spreads out to a large extent, becoming so thin that it becomes unstable and breaks-up. On a heated surface the entire splat is in contact with the substrate so that viscous losses are higher and the splat spreads much less, while cooling faster.

The analytical model of Eq. (9) may also be applied to metallic substrates to estimate the contact area on non-heated metals, if the maximum spread time and spread factors are known. The metals should also be smooth and heated for only short periods of time, since the glass substrates in this study were heated for only a few minutes before spraying. Preheating the metals for very long periods will form an oxide layer, which may affect the model predictions significantly. However, the model will show that on heated surfaces, the area of contact is greatly increased, compared to on non-heated surfaces, possibly due to the absence of adsorbates/condensates on the heated surfaces.

4. Conclusion

The influence of substrate temperature on the area of contact of plasma-sprayed particles was studied. The particles that impacted on a glass surface at room temperature fragmented and splashed, leaving only a small centralized core adhering to the substrate. On a surface held at 400 °C, there was no splashing and a circular splat remained on the surface. The increased splat fragmentation and small contact area on the non-heated surface was attributed to the presence of adsorbates/condensates that created a gas barrier between the splat and the substrate. The increased contact between the splat and the heated substrate increased the viscous dissipation losses, resulting in reduced splat fragmentation and smaller maximum diameters.

A simple conservation of energy analysis was conducted to estimate the splat-substrate contact area on the non-heated substrate. The model predicted that the splat-substrate contact area on the non-heated glass is only about 40% of the splat contact area on the heated glass. Since the extent of splat spreading was much greater on the room-temperature glass, this suggested that only the fluid in the central core of the splat was in contact with the surface, while the rest of the fluid was separated from the substrate by a gas barrier. Validation of the model showed that predictions of the diameter of the central core were within 15% of the core diameters observed in experiments.

References

- [1] S. Costil, H. Liao, A. Gammoudi, C. Coddet, J. Therm. Spray Technol. 14 (2005) 31.
- [2] M. Fukumoto, E. Nishioka, T. Matsubara, Surf. Coat. Technol. 120/121 (1999) 131.
- [3] M. Fukumoto, Y. Huang, M. Ohwatari, in: C. Coddet (Ed.), Thermal Spray: Meeting the Challenges of the 21st Century, Nice, France, May 25–29, 1998, ASM International, 1998, p. 401.
- [4] C. Moreau, J. Bisson, R. Lima, B. Marple, Pure Appl. Chem. 77 (2005) 443.
- [5] N. Mehdizadeh, M. Lamontagne, C. Moreau, S. Chandra, J. Mostaghimi, J. Therm. Spray Technol. 14 (2005) 354.
- [6] H. Zhang, X. Wang, L. Zheng, X. Jiang, Int. J. Heat Mass Transfer 44 (2001) 4579.
- [7] V. Pershin, M. Lufitha, S. Chandra, J. Mostaghimi, J. Therm. Spray Technol. 12 (2003) 370.
- [8] S. Aziz, S. Chandra, Int. J. Heat Mass Transfer 43 (2000) 2841.
- [9] X. Jiang, Y. Wan, H. Hermann, S. Sampath, Thin Solid Films 385 (2001) 132.
- [10] S. Fantassi, M. Vardelle, A. Vardelle, P. Fauchais, J. Therm. Spray Technol. 2 (1993) 379.
- [11] P. Gougeon, C. Moreau, J. Therm. Spray Technol. 10 (2001) 76.
- [12] J. Cedelle, M. Vardelle, B. Pateyron, P. Fauchais, in: E. Lugscheider, C. Berndt (Eds.), Thermal Spray 2004: Advances in Technology and Application, Osaka, Japan, May 10–12, 2004, ASM International, 2004, p. 21.
- [13] L. Bianchi, A. Leger, M. Vardelle, A. Vardelle, P. Fauchais, Thin Solid Films 305 (1997) 35.
- [14] P. Rohan, S. Bouaricha, J. Legoux, C. Moreau, P. Ctibor, S. Nourouzi, A. Vardelle, in: E. Lugscheider, C. Berndt (Eds.), Thermal Spray 2004: Advances in Technology and Application, Osaka, Japan, May 10–12, 2004, ASM International, 2004, p. 382.
- [15] C. Moreau, P. Cielo, M. Lamontagne, S. Dallaire, M. Vardelle, Meas. Sci. Technol. 1 (1990) 807.

- [16] M. Otooni, *Elements of Rapid Solidification: Fundamentals and Applications*, Springer-Verlag, New York, NY, 1998.
- [17] C. Moreau, P. Gougeon, M. Lamontagne, *J. Therm. Spray Technol.* 4 (1995) 25.
- [18] K. Shinoda, Y. Kojima, T. Yoshida, *J. Therm. Spray Technol.* 14 (2005) 511.
- [19] K. Shinoda, A. Yamada, T. Koseki, T. Yoshida, in: J. Mostaghimi, T. Coyle, V. Pershin, H. Salimi-Jazi (Eds.), *17th International Symposium on Plasma Chemistry*, Toronto, Ontario, Canada, August 7–12, 2005, University of Toronto, 2005, p. 914.
- [20] R. McPherson, *Thin Solid Films* 83 (1981) 297.
- [21] N. Ootsuka, T. Goji Etoh, K. Takehara, S. Oki, Y. Takano, Y. Hatsuki, S. Thoroddsen, in: D. Paisley, S. Kleinfelder, D. Snyder, B. Thompson (Eds.), *26th International Congress on High-Speed Photography and Photonics*, Alexandria, VA, USA, September 20, 2004, International Society for Optical Engineering Proceedings, vol. 5580, 2004, p. 153.
- [22] P. Fauchais, M. Fukumoto, A. Vardelle, M. Vardelle, *J. Therm. Spray Technol.* 13 (2004) 1.
- [23] C. Li, J. Li, W. Wang, in: C. Coddet (Ed.), *Thermal Spray: Meeting the Challenges of the 21st Century*, Nice, France, May 25–29, 1998, ASM International, 1998, p. 473.
- [24] C. Moreau, M. Lamontagne, P. Cielo, *Surf. Coat. Technol.* 53 (1992) 107.
- [25] K. Knežević, PhD thesis, Swiss Federal Institute of Technology Zurich, Zurich, 2002.
- [26] S. Chandra, C. Avedisian, *Proc. R. Soc. Lond., A* 432 (1991) 13.
- [27] E. Brandes, G. Brook, *Smithells Metals Reference Book*, 6th ed. Butterworths, Inc., London, England, 1983.
- [28] T. Iida, R. Guthrie, *The Physical Properties of Liquid Metals*, Oxford University Press, Oxford, UK, 1988.
- [29] M. Pasandideh-Fard, Y. Qiao, S. Chandra, J. Mostaghimi, *Phys. Fluids* 8 (1996) 650.